



# Simulation and analysis of light scattering by multilamellar bodies present in the human eye

EMILIA M. MÉNDEZ-AGUILAR,<sup>1,\*</sup> ISMAEL KELLY-PÉREZ,<sup>2</sup> L. R. BERRIEL-VALDOS,<sup>1</sup> AND JOSÉ A. DELGADO-ATENCIO<sup>3</sup>

<sup>1</sup>Department of Optics, Instituto Nacional de Astrofísica, Óptica y Electrónica (INAOE), Luis Enrique Erro No.1, Santa María Tonantzintla, San Pedro Cholula, Puebla, C.P. 72840, México

<sup>2</sup>Centro de Investigaciones en Óptica, Loma del Bosque 115, Colonia Lomas del Campestre León, Guanajuato, C. P. 37150, México

<sup>3</sup>Universidad Politécnica de Tulancingo, Tulancingo, Hidalgo, C.P. 43629, México

\* [mmendez@inaoe.mx](mailto:mmendez@inaoe.mx)

**Abstract:** A modified computational model of the human eye was used to obtain and compare different probability density functions, radial profiles of light pattern distributions, and images of the point spread function formed in the human retina under the presence of different kinds of particles inside crystalline lenses suffering from cataracts. Specifically, this work uses simple particles without shells and multilamellar bodies (MLBs) with shells. The emergence of such particles alters the formation of images on the retina. Moreover, the MLBs change over time, which affects properties such as the refractive index of their shell. Hence, this work not only simulates the presence of such particles but also evaluates the incidence of particle parameters such as particle diameter, particle thickness, and shell refractive index, which are set based on reported experimental values. In addition, two wavelengths (400 nm and 700 nm) are used for light passing through the different layers of the computational model. The effects of these parameters on light scattering are analyzed using the simulation results. Further, in these results, the effects of light scattering on image formation can be seen when single particles, early-stage MLBs, or mature MLBs are incorporated in the model. Finally, it is found that particle diameter has the greatest impact on image formation.

© 2017 Optical Society of America

**OCIS codes:** (290.5850) Scattering, particles; (290.2558) Forward scattering; (330.7329) Visual optics, pathology; (290.4020) Mie theory; (330.7326) Visual optics, modeling.

## References and links

1. WHO, "Blindness: Vision 2020 — The Global Initiative for the Elimination of Avoidable Blindness," (WHO, 2016), <http://www.who.int/mediacentre/factsheets/fs213/en/>.
2. J. Stürmer, "Cataracts — trend and new developments," *Therapeutische Umschau. Revue thérapeutique* **66**, 167–171 (2009).
3. P. A. Asbell, I. Dualan, J. Mindel, D. Brocks, M. Ahmad, and S. Epstein, "Age-related cataract," *Lancet* **365**, 599–609 (2005).
4. P. Murphy and M. D. O'Connor, "Stem cells and the ocular lens: Implications for cataract research and therapy," in *Regenerative Biology of the Eye*, A. Pébay, ed. (Springer, 2014).
5. S. K. Miller, *Adult Nurse Practitioner Certification Review Guide* (Jones & Bartlett Learning, 2012), Chapter 4.
6. V. Nourrit and J. M. Kelly, "Intraocular scatter and visual performances," *Optom. Pract.* **10**, 117–128 (2009).
7. U. R. Acharya, Y. K. E. Ng, and J. S. Suri, *Image Modeling of the Human Eye* (Artech House, 2008), section 1.4.8.
8. C. Delcourt, I. Carriere, M. Delage, P. Barberger-Gateau and W. Schalch, "Plasma lutein, and zeaxanthin and other carotenoids as modifiable risk factors for age-related maculopathy and cataract: The POLA Study," *Invest. Ophthalmol. Visual Sci.* **47**, 2329–2335 (2006).
9. M. Bahrami, M. Hoshino, B. Pierscionek, N. Yagi, J. Regini, and K. Uesugi, "Refractive index degeneration in older lenses: A potential functional correlate to structural changes that underlie cataract formation," *Exp. Eye. Res.* **140**, 19–27 (2015).
10. V. B. Voleti and J. P. Hubschman, "Age-related eye disease," *Maturitas* **75**, 29–33 (2013).
11. R. R. A. Bourne, G. A. Stevens, R. A. White, J. L. Smith, S. R. Flaxman, H. Price, J. B. Jonas, J. Keeffe, J. Leasher, K. Naidoo, K. Pesudovs, S. Resnikoff, and H. R. Taylor, "Causes of vision loss worldwide, 1990–2010: A systematic analysis," *Lancet. Glob. Health.* **1**, 339–349 (2013).
12. H. S. Thomas and J.T.P. van den Berg, "Light scattering model for donor lenses as a function of depth," *Mol. Vis.* **39**, 1437–1445 (1999).

13. A. Mohamed, K. O. Gilliland, S. Metlapally, S. Johnsen, and M. J. Costello, "Simple fixation and storage protocol for preserving the internal structure of intact human donor lenses and extracted human nuclear cataract specimens," *Mol. Vis.* **19**, 2352–2359 (2013).
14. M. J. Costello, S. Johnsen, S. Metlapally, K. O. Gilliland, L. Frame, and D. Balasubramanian, "Multilamellar spherical particles as potential sources of excessive light scattering in human age-related nuclear cataracts," *Exp. Eye. Res.* **91**, 881–889 (2010).
15. M. J. Costello, S. Johnsen, K. O. Gilliland, C. D. Freel, and W. C. Fowler, "Predicted light scattering from particles observed in human age-related nuclear cataracts using Mie scattering theory," *Invest. Ophthalmol. Vis. Sci.* **48**, 303–312 (2007).
16. K. O. Gilliland, S. Johnsen, S. Metlapally, M. J. Costello, B. Ramamurthy, P. V. Krishna, and D. Balasubramanian, "Mie light scattering calculations for an Indian age-related nuclear cataract with a high density of multilamellar bodies," *Mol. Vis.* **14**, 572–582 (2008).
17. M. J. Costello, A. Burette, M. Weber, S. Metlapally, K. O. Gilliland, W. C. Fowler, A. Mohamed, and S. Johnsen, "Electron tomography of fiber cell cytoplasm and dense cores of multilamellar bodies from human age-related nuclear cataracts," *Exp. Eye. Res.* **101**, 72–81 (2012).
18. M. J. Costello, L. A. Brennan, S. Basu, D. Chauss, A. Mohamed, K. O. Gilliland, S. Johnsen, A. S. Menko, and M. Kantorow, "Autophagy and mitophagy participate in ocular lens organelle degradation," *Exp. Eye. Res.* **116**, 141–150 (2013).
19. I. Kelly-Pérez, N. C. Bruce, L. R. Berriel-Valdos, A. Werner, and J. A. Atencio, "Computational model of the effect of light scattering from cataracts in the human eye," *J. Opt. Soc. Am. A* **30**, 2585–2594 (2013).
20. E. Hermans, M. Dubbelman, R. van der Heijde, and R. Heethaar, "The shape of the human lens nucleus with accommodation," *J. Vis.* **7**, 16 (2007).
21. L. Marussich, F. Manns, D. Nankivil, B. Maceo Heilman, Y. Yao, E. Arrieta-Quintero, A. Ho, R. Augusteyn, and J.-M. Parel, "Measurement of crystalline lens volume during accommodation in a lens stretcherlens volume and accommodation," *Invest. Ophthalmol. Vis. Sci.* **56**, 4239 (2015).
22. W. T. Welford, *Aberrations of Optical Systems* (IOP Publishing Ltd., 1986).
23. C. F. Bohren and E. E. Clothiaux, *Fundamentals of Atmospheric Radiation: An Introduction with 400 Problems* (John Wiley & Sons, 2006), Chapter 6.
24. G. D. Eppen and F. J. Gould, *Introductory Management Science: Decision Modeling with Spreadsheets* (Prentice Hall, 1998), Appendix A: Basic Concepts in probability.
25. O. Peña and U. Pal, "Scattering of electromagnetic radiation by a multilayered sphere," *Comput. Phys. Commun.* **180**, 2348–2354 (2009).
26. H. C. Hulst and H. C. V. D. Hulst, *Light Scattering by Small Particles* (Courier Corporation, 1957), Chapters 4 and 9.
27. C. F. Bohren and D. R. Huffman, *Absorption and Scattering of Light by Small Particles* (John Wiley & Sons, 2008), Chapters 3 and 4.
28. O. Boucher, *Atmospheric Aerosols Properties and Climate Impacts* (Springer Netherlands, 2015), Appendix C: Mie theory.
29. W. J. Wiscombe, "Improved Mie scattering algorithms," *Appl. Opt.* **19**, 1505–1509 (1980).
30. W. Yang, "Improved recursive algorithm for light scattering by a multilayered sphere," *Appl. Opt.* **42**, 1710–1720 (2003).
31. A. Chopdar, U. Chakravarthy, and D. Verma, "Age related macular degeneration," *B. M. J.* **326**, 485 (2003).
32. P. Artal, S. Marcos, D. R. Williams, and R. Navarro, "Odd aberrations and double-pass measurements of retinal image quality," *J. Opt. Soc. Am. A* **12**, 195–201 (1995).
33. P. Artal, D. G. Green, I. Iglesias and N. López-Gil, "Double-pass measurements of the retinal-image quality with unequal entrance and exit pupil sizes and the reversibility of the eye's optical system," *J. Opt. Soc. Am. A* **12**, 2358–2366 (1995).

## 1. Introduction

Although cataracts have caused nearly 50% of cases of blindness worldwide [1, 2], the efforts to reduce this disease have not been sufficient and hence cataracts have become an international health concern [3].

The crystalline lens, posterior to the iris and anterior to the vitreous body and retina, has the ability to change the focus between near and far objects [4, 5]. Therefore, any change in the refractive index can potentially be the origin of opacity or clouding. In terms of image formation, this is tantamount to saying that any change in the refractive index interferes with the propagation path when the lens tries to focus on objects. As a result, the quality of the image formation on the retina will be affected [6, 7].

A cataract is defined as some type of opacity or cloudiness caused by any change in the

refractive index [8, 9]. Therefore, this work is focused on scattering particles within the lens, which may interfere with normal vision depending on their size and location [5]. Moreover, the nuclear cataract formation process is slow, gradual, and immutable [5, 10]. The refractive index that makes the lens transparent is achieved by the expression and accumulation of crystallin proteins such as  $\alpha$ -,  $\beta$ -, and  $\gamma$ - crystallins [4]. Hence, any alteration of the structure or composition of the lens can lead to opacity or clouding.

The risk factors that can contribute to the formation of cataracts include gender, illiteracy, ultraviolet light exposure, smoking, rural residency, drinking, an unhealthy lifestyle, trauma, inflammation, vitreoretinal surgery, topical steroid use, and aging [10, 11]. Aging stands out as the most common risk factor for generating cataracts [10]. Depending on the location of the opacity, cataracts can be classified as subcapsular, cortical, or nuclear [12].

Research on crystalline lenses done by Mohamed et al. and Costello et al. [13, 14] found the presence of multilamellar bodies (MLBs) in nuclear cataracts. This type of particles is one of the major sources of scattering in the human nuclei [15]. Scattering is a change in direction of incident light beams due to the presence of particles whose shape, structure, and composition generate changes in the propagation path. Therefore, this work focuses on analyzing the effect of scattering on retinal image formation resulting from changes in the properties of the MLBs. By size, MLBs may be classified as large particles. These particles are hence potential sources for high light scattering because of the low scattering angles that are produced, causing greater modifications to the image formed on the retina. MLBs have a spherical core of cytoplasmic proteins enclosed in multiple lipid-rich bilayers (three to ten bilayers) forming a shell, where the shell thickness ranges from 15 nm to 50 nm [14–17]. The range of the particle diameter is 1–4  $\mu\text{m}$ . Over the course of time, the MLBs could become sufficiently mature, giving rise to two phenomena. In the first case, the MLB core protein condenses, thus increasing its density and decreasing its volume; in the second case, the multiple lipid layers disappear, leaving a thick clear coat [14, 18].

The main interest of the present study is to analyze the effect on image formation of scattering by uncoated single spherical particles, MLBs with a lipid bilayer (with a shell), and mature MLBs. Therefore, this work uses a modified computational model to obtain and compare different probability density functions (PDFs), radial profiles of light pattern distributions, and images of the point spread function (PSF) formed on the human retina in the presence of these particles within the crystalline lens.

## 2. Methods

### 2.1. Simulation model

The effect of scattering, as light enters the eye and passes through particles with a refractive index different to that of the propagating medium before reaching the retina, is simulated by a computer model developed by Kelly et al. [19]. The main ocular structures that are traversed by the light until it reaches the retina are (see Fig. 1): the cornea, aqueous humor, crystalline lens and vitreous humor. The specifications of each structure are described in [19]. Located at the back of the eyeball, the retina is a thin, transparent, and delicate membrane on which the images that pass through the optical media of the eye are focused. It is known that the retina acts as a sensor because it converts these images into electrical signals, which are sent to the brain via the optic nerve. Note that the computational model does not take into consideration absorption as light passes through each medium. This computational model is used to analyze how the image is formed on the retina for a set of light beams with a radius of 0.5 mm, as depicted in Fig. 1.

The particle sizes that were selected for the simulations are derived from data reports in which high concentrations of MLBs have been observed in lenses with nuclear cataracts. According to these reports, the MLB diameters mostly range from 1  $\mu\text{m}$  to 4  $\mu\text{m}$  [14, 15]. For the simulation, the refractive index of the shell was set according to the MLB stage. In order to compute the

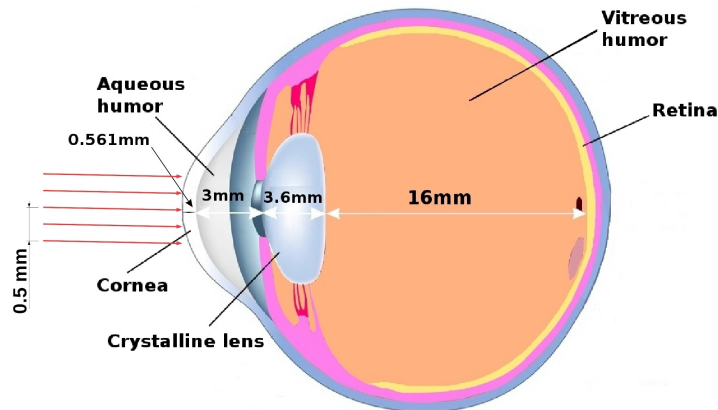


Fig. 1. Structure of the eye with its main elements.

number of particles, calculation of the lens nuclear volume was performed based on [20, 21] and the average geometric parameters of lenses. As a result, the volume of the nucleus in this model is  $45.0626 \text{ mm}^3$ . Measurements carried out by Costello et al. [15] on cataractous lenses collected in the United States found that a typical volumetric density of about 4,071 MLBs per  $\text{mm}^3$ . From these findings, the average number of particles is 183,450 particles. In this research, there is an interest in the effect of light scattering when a considerable number of MLBs are present in the nucleus lens. Hence, the simulation uses more than twice the typical number of particles: namely, 400,000 particles.

## 2.2. Computational Monte Carlo tool for photon propagation

The angles and paths of the photons traversing the eye were calculated using exact ray tracing theory and the Monte Carlo method [19]. On the one hand, exact ray tracing calculates the direction and position of each beam as it passes from one optical medium to another; the important equations of this method are given in [19, 22]. On the other hand, the Monte Carlo method is a numerical method applied to solve a physical problem by the simulation of random variables with the help of a probability density function (PDF) [23]. A PDF is a theoretical model that describes the variation in the results of a random experiment, i.e., the PDF gives the probabilities of all the possible outcomes of a random experiment. The PDF can be obtained from experiments or theoretical models depicting the physical process [24].

### 2.2.1. Calculating PDFs

In this case, the PDF is obtained by the Mie theory [25], and it can be used to describe the direction taken by a photon when it finds particles with a refractive index different to that of the surrounding medium. Once the interaction of the light beams with the scattered particles is simulated, the results appear on a screen that represents the human retina. Based on the shape, size, and distribution of these structures, the Mie solution is used to properly describe the scattering of light caused by these particles [16]. As the wavelength meets the requirement of being smaller than the MLBs, it is possible to use Mie theory to calculate the result of the interaction between the light and MLBs. Solving Maxwell's equations, the results of the Mie solution are obtained [26–28], which allows the change in direction of a beam when it meets a scattered particle to be determined. Thus, a PDF, which gives the direction of a scattered beam, is calculated from the normalized phase function (or normalized scattering function), which is

obtained by applying the Mie theory and has the following form [26, 28]:

$$P(\theta) = \frac{4}{x_L^2 Q_{sca}} \frac{(S_1(\theta)^2 + S_2(\theta)^2)}{2}. \quad (1)$$

The size parameter of the last layer is denoted by  $x_l$  and is defined as  $x_l = 2\pi n_m r_l / \lambda = k r_l$ , for each layer  $l = 1, 2, \dots, L$ ;  $n_m$  is the refractive index of the medium;  $r_l$  is the outer radius of the  $l$ th layer;  $\lambda$  is the wavelength of the incident wave in vacuum; and  $k$  is the propagation constant. In addition,  $Q_{sca}$  is the scattering efficiency, and  $S_1$  and  $S_2$  are the scattering amplitudes, respectively determined by [26–28]:

$$S_1(\theta) = \sum_{n=1}^{\infty} \frac{2n+1}{n(n+1)} [a_n \pi_n(\theta) + b_n \tau_n(\theta)], \quad (2)$$

$$S_2(\theta) = \sum_{n=1}^{\infty} \frac{2n+1}{n(n+1)} [a_n \tau_n(\theta) + b_n \pi_n(\theta)]. \quad (3)$$

The key parameters of the Mie calculations are the so-called Mie coefficients or scattering coefficients ( $a_n$  and  $b_n$ ), which are used to determine the scattering amplitude functions. The variables  $\pi_n$  and  $\tau_n$  are the angular functions, which can be established from the recurrence relations [25, 29]. This work uses the scattering series of a  $l$ -layered sphere to construct these coefficients [25, 30]. Hence, to calculate the scattering coefficients, it is necessary to know the Riccati-Bessel functions ( $\psi_n$  and  $\xi_n$ ) as well as the relative refractive index of the last layer ( $m_L$ ), which is defined as  $m_l = n_l/n_m$ , where  $n_l$  is the refractive index outside of the particle with the  $l$ th component. More details about these parameters can be found in [25].

Finally, scattering efficiency factor  $Q_{sca}$  is obtained by the following equation [26, 27]:

$$Q_{sca} = \frac{2}{x_L^2} \sum_{n=1}^{\infty} (2n+1) [|a_n|^2 + |b_n|^2]. \quad (4)$$

Parameters such as the particle radius, wavelength, and relative refractive index contribute significantly to the scattering effect. Therefore, it is important to control these parameters; however, these parameters are sometimes unworkable or difficult to control experimentally. Consequently, computational modeling is a good option for analyzing the effects of light scattering on image formation in relation to variations in these parameters.

### 2.3. Simulations

Experimental values obtained by Costello et al. [14, 15] for parameters such as the diameters and refractive index of the MLBs were used in the simulations. Figure 2 shows the different types of particles implemented in the simulations. The particle diameter ranged from 1  $\mu\text{m}$  to 4  $\mu\text{m}$ . Single-particle refractive indices were 1.49 and 1.42 for the core and the surrounding cytoplasm, respectively (Fig. 2(a)) [15]. For MLBs with a lipid bilayer, the refractive indices were 1.49 in the core, 1.50 in the lipid bilayer shell, and 1.42 in the surrounding cytoplasm (Fig. 2(b)) [14]. The refractive indices of the MBL particles in mature stage were 1.49 in the core, 1.35 in a shell with cortical cytoplasm (as a dilute protein solution with water), and 1.42 in the surrounding cytoplasm (Fig. 2(c)) [14, 17]. In addition, this work used two different wavelengths, 400 nm and 700 nm. Consequently,  $m_1 = n_i/n_c = 1.49/1.42$  for single particles;  $m_1 = n_l/n_m = n_i/n_{lb} = 1.49/1.5$  and  $m_2 = n_l/n_m = n_{lb}/n_c = 1.5/1.42$  for MLBs with a lipid bilayer shell; and  $m_1 = n_l/n_m = n_i/n_m = 1.49/1.35$  and  $m_2 = n_l/n_m = n_m/n_c = 1.35/1.42$  for a mature MLB shell.

The model and method presented in Sections 2.1 and 2.2 were used to determine the effects of changing some of the parameters of the three types of particles. Particle diameter is one of

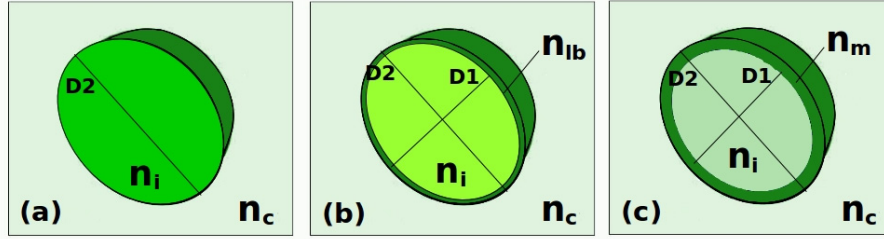


Fig. 2. Diagrams of the particles. (a) Particles with no shell, (b) particles with lipid multilamellar shells (MLBs), and (c) particles representing mature MLBs with an enlarged low density shell without lipids. The refractive indices of the particles are 1.49 and 1.42 for the core ( $n_i$ ) and the surrounding cytoplasm ( $n_c$ ), respectively. For the MLBs, the refractive indices of the shells are 1.50 for the lipid bilayer ( $n_{lb}$ ) and 1.35 for shells of mature MLBs ( $n_m$ ). Hence,  $D_1$  is the diameter of the core and  $D_2$  is the diameter of the entire particle.

the variables in the simulations. The values used for the largest diameter ( $D_2$ ) were 1, 2, 3, and 4  $\mu\text{m}$ . For MLBs with lipid bilayers and mature MLBs, the diameter values include the shell or coating around the core. Hence, a shell with a thickness of zero ( $S = 0$  nm) is considered for single particles, a shell with thickness of 50 nm ( $S_{lb} = 50$  nm) is considered for lipid bilayers, and a shell with thickness of 200 nm ( $S_m = 200$  nm) is considered for MLBs in the mature state. The other parameter is the wavelength. In all cases, 1,000,000 photons were emitted to form the set of light beams with wavelengths of 400 nm and 700 nm. These wavelengths were chosen because they are values at the boundaries of the visible light spectrum.

Effects caused by the variation in a single factor or parameter can be obtained by computer simulations of the human optical system. Therefore, the effect on retinal image formation can be evaluated using these simulations.

### 2.3.1. Obtaining PDFs

The PDF for determining the angle at which a beam is scattered is described using the normalized propagation phase function. In order to normalize the propagation phase function ( $P(\theta)$ ), it is necessary to find a function whose integral over all the angles is equal to one, as in the following example:

$$\frac{1}{4\pi} \int_0^{2\pi} \int_0^\pi P'(\theta) \sin\theta d\theta d\varphi = 1, \quad (5)$$

Because it is assumed that the azimuth angle is uniformly distributed in  $[0, 2\pi]$ , function  $P(\theta)$  does not depend on  $\varphi$ . Therefore,

$$\frac{1}{2} \int_0^\pi F(\theta) \sin\theta d\theta = 1, \quad (6)$$

Next, a function that is derivable from the propagation phase function and meets these conditions must be found. Such a function can have the following form:

$$F(\theta) = \frac{P(\theta)}{\frac{1}{2} \int_0^\pi P(\theta) \sin\theta d\theta}, \quad (7)$$

Because the propagation phase function is obtained for a finite number of discrete angles, the denominator of Eq. (7) can be calculated as the sum

$$S = \frac{1}{2} \sum_{i=1}^{N_\theta} P_i \sin\theta_i \Delta\theta_i. \quad (8)$$

Hence, the normalized phase function can be constructed as follows:

$$P_N = \frac{P_i \sin \theta_i}{2S}. \quad (9)$$

Finally, summation of the normalized phase function over all the angles yields

$$\sum_{i=1}^{N_\theta} P_N = 1. \quad (10)$$

### 2.3.2. Obtaining radial profiles

Once the simulations have been carried out, it is possible to observe the effects of light scattering on the images that form in the retina and to quantify these effects in terms of the extended-point function. The results are stored in an array whose elements have the number of photons that fall within the limits of a certain segment of the central region of the retina. Using these results, the image of a point spread can be divided into concentric rings. Each ring is formed by an array of elements that meet the condition of being at a certain distance from the center. The center of these rings corresponds to the center of the image whose value regularly has the maximum value within this matrix. The next step is to add the values of the elements forming each ring, and to then divide this total by the number of elements of the respective ring. Subsequently, a vector that describes the behavior of the average radial intensity when moving away from the center of the image can be obtained. The resulting vector for each simulation is appointed as the radial profile.

## 3. Results

### 3.1. Results of the PDFs

The first step was to obtain the behavior of the PDFs by varying different parameters to observe how the angular distribution of the photons after scattering is affected by the structural properties of the particles and wavelength. Figure 3 shows a local maximum of the PDF at  $7.75^\circ$  for shell-less particles. A second prominent maximum is located at  $26^\circ$  for particles with shells 200 nm thick. The third maximum, at  $20.75^\circ$ , corresponds to particles with a lipid bilayer shell with a thickness of 50 nm. These three maxima were obtained from simulations using a wavelength of 400 nm. The other maxima correspond to the results obtained using a wavelength of 700 nm. At this wavelength, the maximum at  $36.5^\circ$  for a shell thickness of 50 nm is greater than the maximum for a shell thickness of 200 nm. Then, the order of the maxima is reversed when the wavelength passes from 400 nm to 700 nm and when the particles have a shell. In contrast, a local maximum before the global maximum is observed when there is some kind of shell on the particles. In addition, the influence of the wavelength on the PDFs at shorter wavelengths can be seen in Fig. 3. The number of oscillations of the PDFs at a wavelength of 400 nm is greater than it is at 700 nm. Specifically, the PDF obtained using particles with a shell thickness of 50 nm presents five oscillations at 400 nm, whereas only two oscillations occur at 700 nm. Furthermore, maxima at a wavelength of 700 nm exhibit wider oscillations, especially when the shell thickness is 200 nm.

Figure 4 shows that there are no oscillations before the maximum, as happened in the case of particles of 1  $\mu\text{m}$  diameter in Fig. 3. In this same figure, there is a PDF maximum at  $3.5^\circ$  for particles with a shell thickness of 50 nm. Moreover, a second important maximum is found at  $3.5^\circ$  for shell-less particles, differing from the first one only by a value of 0.0016. The third maximum at  $5.25^\circ$  is observed in the PDF for particles with a shell thickness of 200 nm. These three maxima were acquired from simulations using a wavelength of 400 nm. The same behavior is observed in the results of the simulations using a wavelength of 700 nm. Furthermore, the

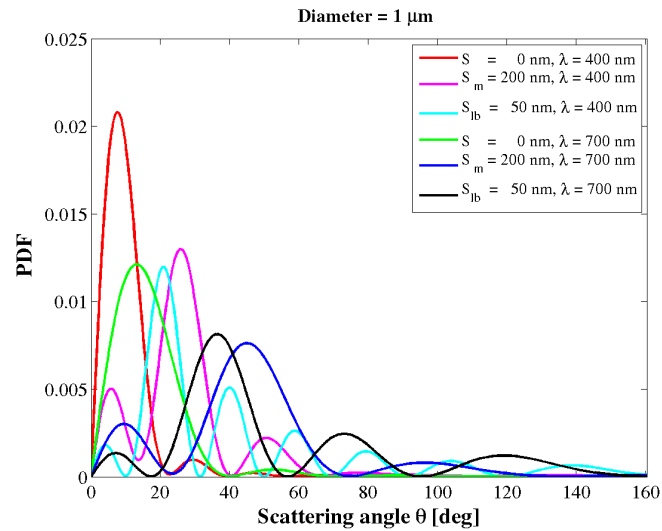


Fig. 3. Scattering angle versus PDF using a particle a diameter of 1 μm and with different shell thicknesses.

maximum for particles with a shell thickness of 50 nm and the maximum for shell-less particles are similar at a wavelength of 700 nm. However, the maximum for particles with shell thickness of 200 nm is different to the above cases: their PDF is lower and wider. Additionally, there are more oscillations at a wavelength of 400 nm. Finally, it is observed that the oscillations are narrower for a particle diameter of 2 μm than for a diameter of 1 μm.

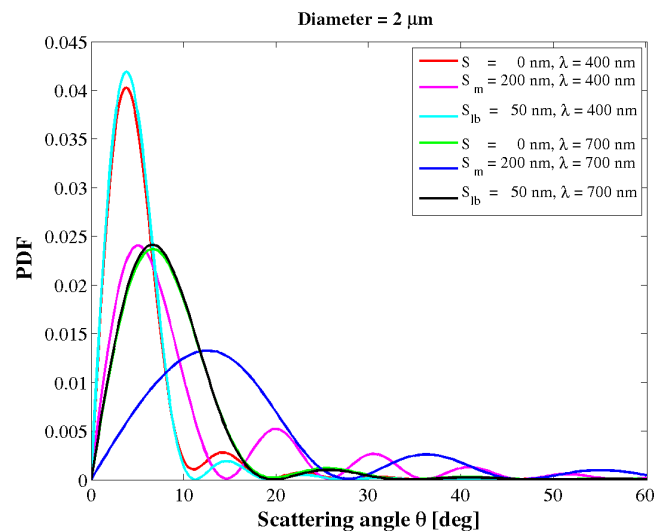


Fig. 4. Scattering angle versus PDF using a particle a diameter of 2 μm and with different shell thicknesses.

The three maxima of the PDFs for a wavelength of 400 nm are observed at  $2.5^\circ$  in Fig. 5. The greatest maximum corresponds to the PDF for particles with a shell thickness of 50 nm, followed by that for shell-less particles and that for particles with a shell thickness of 200 nm.

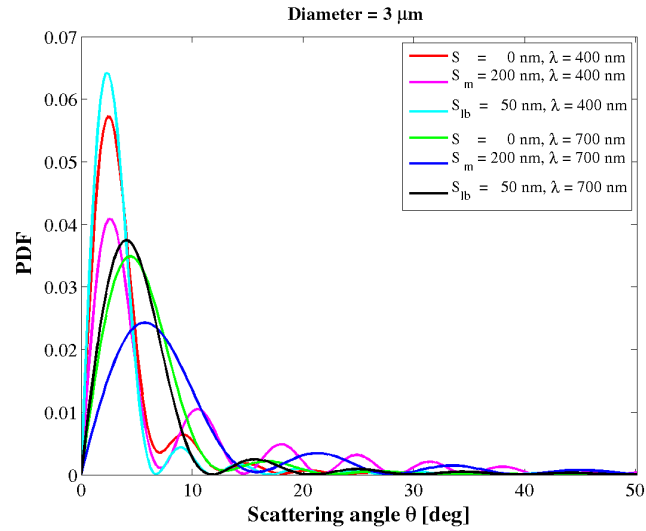


Fig. 5. Scattering angle versus PDF using a particle a diameter of  $3 \mu\text{m}$  and with different shell thicknesses.

By comparison, the maxima of the PDFs simulated at 700 nm are lower in magnitude than those at 400 nm; however, they have the same trend. More oscillations are observed at wavelength 400 nm again. Regarding the width of the oscillation at the wavelength of 700 nm, the first oscillation of the PDF for particles with a shell thickness of 200 nm is larger than those corresponding to the PDFs for particles without a shell and those with a shell thickness of 50 nm. Furthermore,

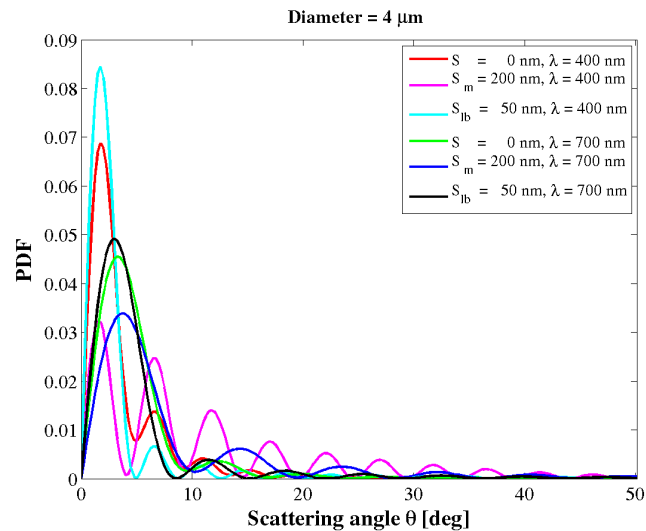


Fig. 6. Scattering angle versus PDF using a particle a diameter of  $4 \mu\text{m}$  and with different shell thicknesses.

the amplitudes of the oscillations of the PDFs corresponding to maxima in Fig. 5 are lower than those observed in Figs. 3 and 4.

The PDFs in Fig. 6 are part of the results for a particle diameter of  $4 \mu\text{m}$ . In these results, all

maxima occur at scattering angles below  $10^\circ$ . Note that the highest maximum for a wavelength of 400 nm corresponds to the simulation for a shell thickness of 50 nm and the lowest maximum corresponds to simulations for a shell thickness of 200 nm. However, for a wavelength of 700 nm, the maxima are close with respect to the scattering angle. Here again, the number of oscillations is higher at a wavelength of 400 nm. Besides, the widths of the oscillations are narrower than for previous cases (particle diameters of 1, 2, and 3  $\mu\text{m}$ ).

### 3.2. Results of radial profiles

Once the PDFs are obtained, it is possible to simulate the photon path through the different layers and the particles scattering light in the eye to reach the retina. The intensity distribution on the retina is described using radial profiles. Because variations in the particle parameters are reflected in these profiles, the next step is to obtain the radial profiles under different particle parameters. Then, the diameter of the particles is varied again. By increasing the particle diameter, the scattering of the light becomes mainly directed at smaller angles in a forward direction; hence, more scattered photons reach the central region of the retinal image plane.

As a result, the intensity distribution of the light scattered down to the central region in all cases increases with particle size. The effect of scattering due to the increase in light intensity can be seen on the edges of the PDF, which generates a veiling light as the particle size increases.

Figure 7 encompasses the radial profiles corresponding to particles with a diameter of 1  $\mu\text{m}$  at wavelengths of 400 nm and 700 nm. According to these profiles, there are small variations among them in term of their behaviors, except for the profile simulated using a wavelength of 400 nm for particles with a shell of thickness 50 nm, which declines from a radial distance of 2.25 mm. The profiles corresponding to simulations using shell-less particles, as in the respective PDFs, present few oscillations. Regarding simulations at 700-nm wavelengths, their radial profiles have more fluctuations; however, the fluctuations are small because their intensity range is low (from  $10^{-2}$  to  $10^0$ ). The decline in intensity in the radial profiles may be related to the number of oscillations in the PDFs. For example, the radial profile corresponding to a shell of 50 nm at a wavelength of 400 nm has a greater decline in intensity, and its PDF has a larger number of oscillations.

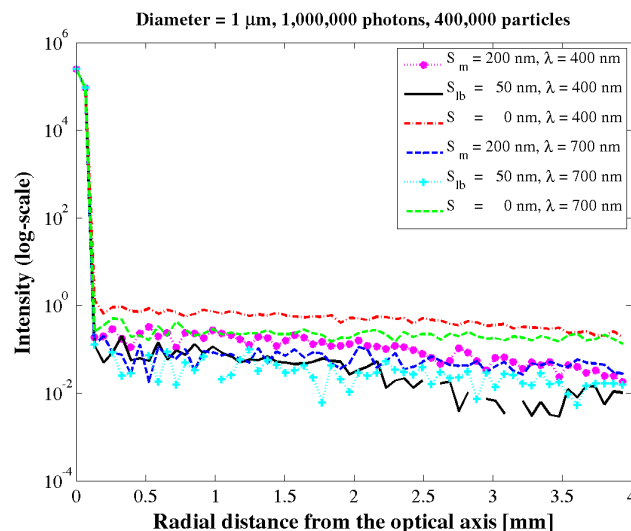


Fig. 7. Radial intensity profiles in the retinal plane with MLB shell thicknesses of 0, 50, and 200 nm and diameter  $D_2 = 1 \mu\text{m}$ .

The radial profiles from simulations using particles with a diameter of  $2\ \mu\text{m}$  are shown in Fig. 8. The profiles where the particles have a shell thickness of zero or 50 nm and the wavelength is 400 nm exhibit similar behavior up to 3.25 mm. Beyond 3.25 mm, the profile obtained using shell-less particles has an intensity slightly greater than that of particles with a shell thickness of 50 nm. However, the resulting radial profiles from incorporating particles without shell and with shells 50-nm thick and using a wavelength of 700 nm approach the same values: 0 mm to 4 mm. Additionally, after the first maximum, the profiles with the particles with shell thicknesses of 200 nm show less light scattering intensity than those of the particles with no shells or shells 50-nm thick, taking into account the same wavelength of 400 nm. Then, around 2.4 mm, the radial profiles begin overlapping and from this point, the radial profile corresponding to particles with a shell thickness of 200 nm has a higher degree of scattering along the entire radial distance in relation to the other two radial profiles. In contrast, the radial profiles obtained from incorporating particles with a shell thickness of 200 nm at a wavelength of 400 nm and particles with no shells or shells 50-nm thick at a wavelength of 700 nm have the same behavior up to 1.8 mm. Finally, the radial profile corresponding to particles with a shell thickness of 200 nm and a wavelength of 700 nm remains almost constant with small fluctuations. The results presented in Fig. 8 show that, along the horizontal axis, the intensity decreases in the radial profiles of the simulations for shell-less particles and for particles with a shell thickness of 50 nm. This decrease is more marked from 2.25 mm to the maximum radial distance. The last effect may be related to the number of oscillations in the PDF, where, when a wavelength of 400 nm is used, more oscillations appear.

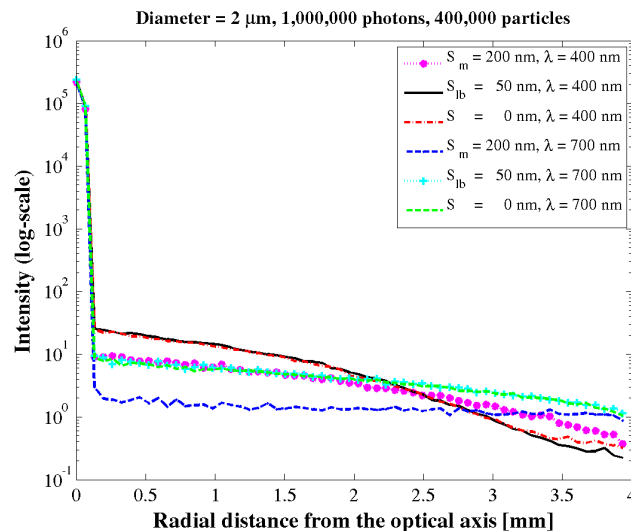


Fig. 8. Radial intensity profiles in the retinal plane with MLB shell thicknesses of 0, 50, and 200 nm and diameter  $D_2 = 2\ \mu\text{m}$ .

The radial profiles from simulations that incorporated particles with a diameter of  $3\ \mu\text{m}$  are shown in the Fig. 9. The radial profiles of simulations executed at a wavelength of 400 nm have the same behavior until 2.8 mm. Beyond this radial distance, the radial profiles overlap and adopt different trends. Specifically, beyond 2.8 mm, the radial profile involving particles with a shell thickness of 200 nm reaches greater intensity than the radial profiles corresponding to particles without a shell or those with a shell of 50 nm. In addition, a concavity appears in these profiles in the radial distance range of 1.5 mm to 2.57 mm, which represents a fringe of low intensity.

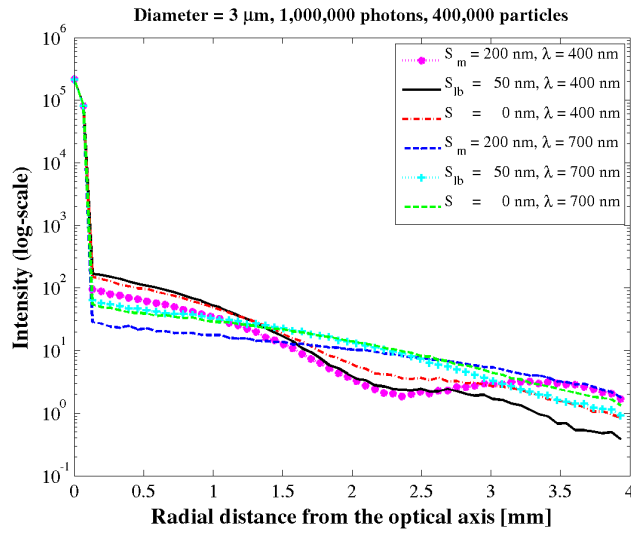


Fig. 9. Radial intensity profiles in the retinal plane with MLBs shell thicknesses of 0, 50, and 200 nm and diameter  $D_2 = 3 \mu\text{m}$ .

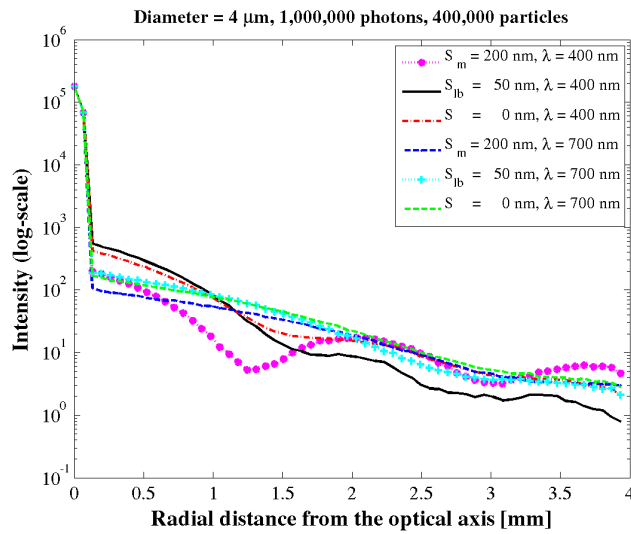


Fig. 10. Radial intensity profiles in the retinal plane with MLBs shell thicknesses of 0, 50, and 200 nm and diameter  $D_2 = 4 \mu\text{m}$ .

The lower intensity in this range is observed when particles with 200-nm thick shells are used. In contrast, the results using a wavelength of 700 nm show that the radial profiles obtained by simulations including shell-less particles and those with a shell thickness of 50 nm have the same trend up to 2.5 mm of radial distance, where the radial profiles overlap. The radial profile for particles with a shell thickness of 200 nm show lower values of intensity in the range 0.2 mm to 2.1 mm. Emphasizing this, after 2.5 mm, the highest intensity corresponds to the radial profile for particles with a shell of 200 nm, whereas the lowest intensity corresponds to the radial profile for particles with a shell of 50 nm.

The radial profiles simulated using particles with an external diameter ( $D_2$ ) of 4  $\mu\text{m}$  are shown in Fig. 10. Clearly, the radial profiles undergo various overlaps in the radial distance range under consideration. On the one hand, at a wavelength of 400 nm, the highest intensity at a short radial distance corresponds to the radial profile involving particles with a shell thickness of 50 nm. Subsequently, in the radial distance ranges 1.15–1.75 mm and 2.80–3.30 mm, the highest intensity is reached by the radial profile corresponding to the simulation for shell-less particles. In the ranges 1.75–2.80 mm and 3.30–4.00 mm, the highest intensity is reached by the radial profile corresponding to particle shells 200-nm thick. In contrast, at a wavelength of 700 nm, the three cases follow approximately the same trend up to 1.5 mm. With respect to intensity, at a radial distance lower than 1.5 mm, the highest intensity corresponds to the radial profile for particles with a shell thickness of 50 nm, whereas the lowest intensity corresponds to the use of particles with a shell thickness of 200 nm. From around 1.5 mm, the radial profile for the shell-less particle simulations show higher intensity values.

#### 4. Discussion and conclusions

The effect of light scattering when MLBs are present in the human eye was studied using a computational model that simulates the different layers traversed by the light to reach the retina. This model uses a PDF to describe the interaction between light and MLBs. However, the interaction also depends on the wavelength. Accordingly the simulations were set at two different wavelengths (400 nm and 700 nm). The results show that all studied factors (the MLB parameters and the wavelength of the incident light) generated changes in the PDF response. Note that the most influential parameter was the diameter of the MLBs. In the presence of larger particles, light propagates at smaller angles, and consequently, greater forward scattering is generated. If the diameter of the particles increases, the scattering effect in the central region of the image also increases. In other words, the larger the particles are, the probability that the light is scattered at angles less than  $90^\circ$  is higher.

After simulating and analyzing the results of the PDF, the same set of parameters (diameter, shell thickness, wavelength, and refractive index) was used in the simulation of the computational model, which includes all layers of the eye considered in this work. As result, the radial profiles corresponding to each case of image formation were obtained. The results show some interesting patterns in the radial profiles that are worth mentioning. The profiles corresponding to simulations for MLBs with a lipid bilayer ( $S_{lb} = 50$  nm) and single particles ( $S = 0$ ) have similar values of intensity up to a certain radial distance. This proximity decreases as the particle diameter increases, except for a diameter of 1  $\mu\text{m}$ . In this case, the profiles have different trends, intensities, and amplitude of the fluctuations. The radial profiles corresponding to simulations including mature MLBs ( $S_m = 200$  nm) with diameters of 2, 3, and 4  $\mu\text{m}$  exhibit the same behavior as in the previous cases; however, their intensities are lower than the others up to a certain radial distance. Beyond this point, they become higher. This last effect would show up on the retinal plane as an increase in scattered light for radial distances farther from the central point. Furthermore, as the MLB diameter increases, oscillations in the intensity begin to appear, giving rise to greater changes in the radial profiles. Taking into account the wavelength, the length of the oscillations is small in the PDFs for a wavelength of 700 nm. Therefore, fewer

oscillations are observed in the radial profiles obtained at this wavelength. In order to better understand the effect of particle diameter, images of the PSF are included. Figures 11 and 12 show images with the PSF for cases where the diameter of simple particles is varied (1, 2, 3, and 4  $\mu\text{m}$ ) using the wavelengths of 400 nm and 700 nm, respectively.

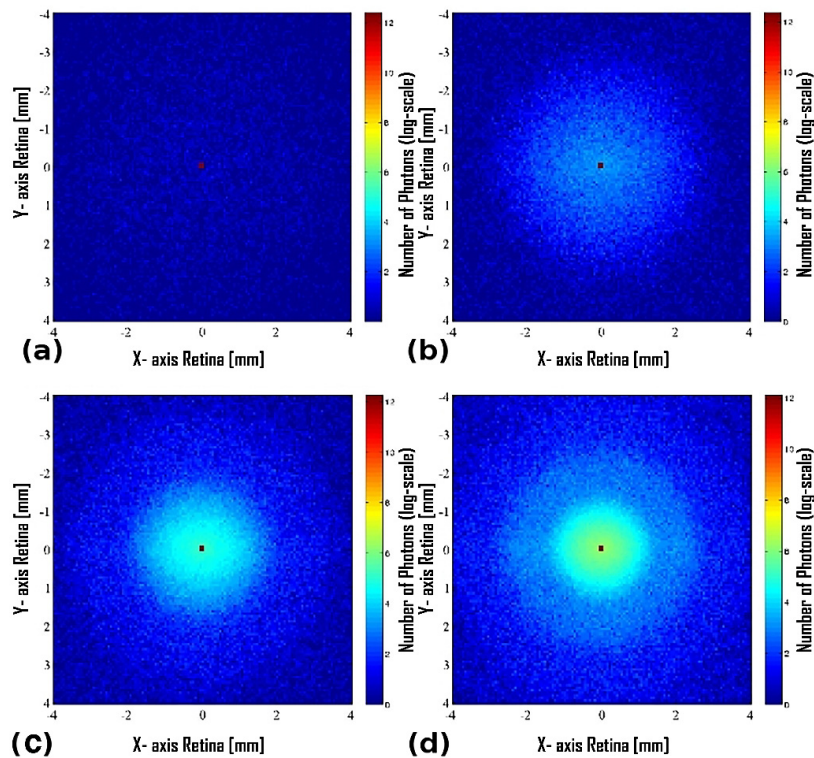


Fig. 11. Changes of the light intensity distribution on the retina plane as the particle size is varied, using a wavelength of 400 nm, 400,000 particles, and 1,000,000 photons. (a)  $D_2 = 1 \mu\text{m}$ . (b)  $D_2 = 2 \mu\text{m}$ . (c)  $D_2 = 3 \mu\text{m}$ . (d)  $D_2 = 4 \mu\text{m}$ .

According to Figs. 11 and 12, few photons are scattered when the diameter of the particles inside the crystalline lens is 1  $\mu\text{m}$ . As the diameter increases, photons are increasingly scattered around the center of the retina (macula). Recall here that the average size of the macula covers an area corresponding to a circle of 5.5 mm in diameter [31]. The main difference between the PSFs at wavelengths 400 nm and 700 nm is that fewer photons are scattered onto the retina at 700 nm.

Based on an overall review of the PDFs, radial profiles, and PSF images, the particle diameter is the parameter that most affects retinal image formation. Nevertheless, given the discrepancies in the experimental measurements of the refractive indices of the particle core and the medium, it is also important to evaluate the effect of variations in these indices on image formation, keeping them within the range of values reported.

An experimental technique like the double pass method [32,33] gives insight into the forward and backward scattering behavior of spherical particles. Because of the structure and size of the MLBs, it is complicated to do this experimentally.

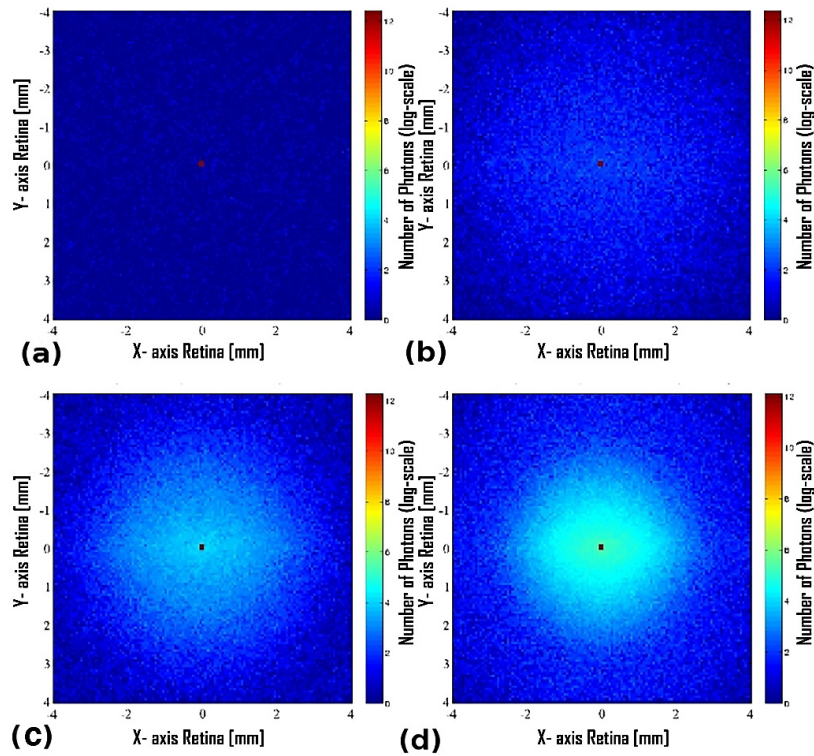


Fig. 12. Changes of the light intensity distribution on the retina plane as the particle size is varied, using a wavelength of 700 nm, 400,000 particles, and 1,000,000 photons. (a)  $D_2 = 1 \mu\text{m}$ . (b)  $D_2 = 2 \mu\text{m}$ . (c)  $D_2 = 3 \mu\text{m}$ . (d)  $D_2 = 4 \mu\text{m}$ .

A particle manufacturing process with the physical characteristics of the MLBs would be very complex for the experimental measurement of scattering effects induced directly in image formation. However, computational simulation proves to be a convenient alternative for studying the effect caused by this type of particle in media such as human ocular tissues. This research generates valuable information to understand the effects of MLBs on retinal image formation. The results obtained with extended point functions provide information that can be used to understand the effects of cataracts.

The results show that prominent forward scattering heavily controls the scattering at the retina when particles larger than  $1 \mu\text{m}$  in diameter are included. These findings could be of value for ophthalmologists examining *in vivo* age-related cataracts. Normally, ophthalmologists examine an eye with a slit lamp. Using this technique, the backward scattering produced by smaller particles than MLBs is observed. When particle size, defined as  $x = 2\pi r/\lambda$  (where  $r$  is the radius of the particle and  $\lambda$  is the wavelength), is smaller in relation to the wavelengths within the visible range (particle size  $< 1/10 \lambda$ ), it can be considered a small particle and modelled using Rayleigh scattering [15]. Small particles contribute fundamentally at angles greater than  $90^\circ$  (high-angle scattering); hence, a smaller amount of light reaches the retina and the image is dimmer [14, 15]. Nevertheless, from the results obtained with the simulations, it can be observed that MBLs have a special role in the generation of forward scattering at the retina, which causes

the point spread function to deteriorate.

### **Funding**

Department of Optics, Instituto Nacional de Astrofísica; Óptica y Electrónica (INAOE); Consejo Nacional de Ciencia y Tecnología (CONACYT).

### **Acknowledgment**

We would like to express our gratitude to professor Teresa Sullivan, José Luis Herrera Celis, Ph.D. and Marcus Edward Smith, Ph.D. (Peace Corps USA, Universidad Politécnica de Tulancingo) for reviewing this work.